SANDIA REPORT
SAND2019-9384

Printed August 8, 2019

Sandia National Laboratories

EMPIRE-PIC Code Verification of a Cold Diode

T. M. Smith, T. D. Pointon, K. L. Cartwright, W. J. Rider

Prepared by
Sandia National Laboratories
Albuquerque, New Mexico 87185
Livermore, California 94550

Issued by Sandia National Laboratories, operated for the United States Department of Energy by National Technology & Engineering Solutions of Sandia, LLC.

Available to DOE and DOE contractors from

U.S. Department of Energy
Office of Scientific and Technical Information
P.O. Box 62
Oak Ridge, TN 37831

Telephone: (865) 576-8401
Facsimile: (865) 576-5728
E-Mail: reports@osti.gov
Online ordering: http://www.osti.gov/scitech

Available to the public from

U.S. Department of Commerce
National Technical Information Service
5301 Shawnee Road
Alexandria, VA 22312

Telephone: (800) 553-6847
Facsimile: (703) 605-6900
E-Mail: orders@ntis.gov
Online order: https://classic.ntis.gov/help/order-methods

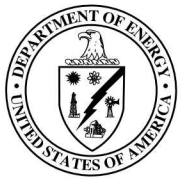

ABSTRACT

This report presents the code verification of EMPIRE-PIC to the analytic solution to a cold diode which was first derived by Jaffé[1]. The cold diode was simulated using EMPIRE-PIC and the error norms were computed based on the Jaffé solution. The diode geometry is one-dimensional and uses the EMPIRE electrostatic field solver. After a transient start-up phase as the electrons first cross the anode-cathode gap, the simulations reach an equilibrium where the electric potential and electric field are approximately steady. The expected spatial order of convergence for potential, electric field and particle velocity are observed.

CONTENTS

LIST OF FIGURES

LIST OF TABLES

SUMMARY

The cold diode problem consists of a one-dimensional, anode-cathode gap, with an applied voltage across this gap, and particles emitted at one end. Jaffé [1] derived an analytic solution to this problem. This has been simulated with EMPIRE-PIC and compared to the analytic solution to perform formal code verification. An electrostatic approximation consistent with Jaffé's solution was used in the PIC simulations. The simulations were run until an equilibrium state is reached, and then this state was analyzed. The error was defined as the absolute difference between the analytic solution and the computed PIC solution at the final time at all spatial locations of a single row of mesh cells.

Two beam emission strategies; uniform in timestep sub-interval and random in timestep sub-interval were examined. For uniform particle emission, the expected order of accuracy ($p \approx 2$) was observed for three quantities of interest; electric potential, electric field and particle velocity. Using a constant timestep that was an integral divisor of the particle transit time, relatively few particles per timestep emitted were required. In the case of random particle emission, expected orders of accuracy ($p \approx 2$) were also observed for the three quantities of interest using a much larger number particles emitted per timestep.

This analysis highlighted a deficiency in the E-field value at boundaries that caused degradation of the convergence rates for L_1 and L_∞ error norms. This problem had been a known issue in EMPIRE, but the clear lack of convergence for this simple problem helped to motivate a prompt correction. Once the E-field boundary correction was implemented by the EMPIRE-PIC development team, the expected order of accuracy was achieved in all three error norms.

It was shown that Leapfrog time integration produced first-order accuracy for all three velocity error norms due to a known issue with the algorithm where particle position and velocity are out of sync by half a timestep at the end of each timestep. A correction to the velocity error when applied to the error estimation recovers second-order accuracy. A new time integration algorithm (Velocity-Verlet[2]) was implemented that produces syncronized particle position and velocity at the end of each timestep, therefore not requiring a correction. With Velocity-Verlet the expected order-of-accuracy were observed without any corrections.

1. INTRODUCTION

A key component in the production of high-current charged particle beams is the diode, consisting of an anode-cathode ("AK") gap, with a large voltage applied between them. Given appropriate particle sources at the emitting electrode (cathode for electrons, anode for ions), high-current beams can be extracted from the other electrode.

A related problem is the emission of photo-electrons on the inside of a cavity subjected to an intense burst of X-rays incident on the cavity exterior. The distribution of electrons emitted depends on the spectrum of photons and the material that the photons have gone through. However, a simplified problem is where the electron distribution is a δ-function which is the case that is done in this report.

The simplest starting point for analysis of both of these systems is the 1D planar diode, neglecting all the multi-dimensional geometric complications. We consider a 1D AK gap, $0 \leq x \leq d$, with a voltage V applied across it. A cold beam of particles of charge q, and mass m is injected at $x = 0$, all particles with initial kinetic energy W. An equilibrium solution for the beam density, $n(x)$, beam velocity $v(x)$, and electrostatic potential $\phi(x)$ must satisfy the equations:

$$J = nqv = const, \text{ charge conservation,} \tag{1.1}$$

$$\tfrac{1}{2}mv^2 + q\phi = W, \text{ energy conservation, and} \tag{1.2}$$

$$\frac{d^2\phi}{dx^2} = -\frac{qn}{\epsilon_0}, \text{ Poisson's equation.} \tag{1.3}$$

We use MKS units throughout this paper (with the exception of usually using electron-volts for energy). In Equation 1.3, ϵ_0 is the permittivity of free space. The boundary conditions on the potential are $\phi(0) = 0$ and $\phi(d) = V$. The particles are accelerated across the gap if $qV < 0$. In Equation 1.2 we neglect relativistic effects, requiring $qV \ll mc^2$. For electrons, this means $V \ll 511\ keV$.

A key feature of the analysis is that there is a limiting maximum current density J for which an equilibrium solution exists. As the space-charge of the beam increases, the resulting electric field from Poisson's equation decelerates the particles, and eventually reaches the point at which they are turned back towards the emission surface. For this reason, the limiting current is called the Space-Charge-Limited (SCL) current.

For application to diodes, an important special case is $W = 0$ and $qV < 0$. This case has a simple solution for the SCL current, known as the "Child-Langmuir" current [3, 4],

$$J_{CL} = \frac{4}{9}\epsilon_0 \left(\frac{2|q|}{m}\right)^{1/2} \frac{|V|^{3/2}}{d^2}. \tag{1.4}$$

As the current is increased up to J_{CL}, the space-charge of the beam reduces the electric field at the emission surface below it's vacuum value of V/d. At J_{CL}, the electric field at the surface drops to zero, and for $J > J_{CL}$, there is no equilibrium solution.

A second important special case is $W > 0$ and $V = 0$, injecting a cold beam into a grounded box. This is an important limiting case of the photo-electrons injected into a cavity or a high velocity beam entering a drift section through a foil. The solution is clearly symmetric about $x = d/2$. A naive approach to compute the SCL current is to assume that it must be such that $v = 0$ at $x = d/2$. Then we can apply the Child-Languir equation to a "diode" with gap $d/2$ and voltage W/q, giving

$$J_0 = \frac{16}{9}\epsilon_0 \left(\frac{2|q|}{m}\right)^{1/2} \frac{|W/q|^{3/2}}{d^2}. \tag{1.5}$$

This solution is **not** correct, although J_0 is a useful quantity for defining the actual SCL current. The problem with the naive approach is that the boundary conditions are not correctly satisfied.

The solution to the full cold diode problem with $W \neq 0$ and/or $V \neq 0$ was published back in 1944 by George Jaffé [1]. This old paper is a very hard read, particularly because of confusing nomenclature, but the results are absolutely correct!

The outline of this report is as follows. In Section 2, we present the Jaffé cold diode theory. In Section 3 we present a EMPIRE-PIC code verification study that relies on the analytic solution to the Jaffé cold diode theory. In Section 4 we discuss physical relevance and in the final Section 5 we draw conclusions.

2. JAFFÉ COLD DIODE THEORY

We start by combining Equations 1.1 - 1.3 into a single, non-linear 2nd-order ODE for $\phi(x)$,

$$\frac{d^2\phi}{dx^2} = -\frac{J}{\epsilon_0}\left[\frac{2}{m}(W - q\phi)\right]^{-1/2}. \tag{2.1}$$

Then define dimensionless variables,

$$g = \frac{x}{d}, \text{ and } f = \frac{q\phi}{W}. \tag{2.2}$$

This transforms Equation 2.1 into the dimensionless equation,

$$\frac{d^2 f}{dg^2} = -K(1-f)^{-1/2}, \tag{2.3}$$

where

$$K = \frac{16}{9}\frac{J}{J_0}. \tag{2.4}$$

Equation (2.3) is subject to the boundary conditions $f(g=0) = 0$ and $f(g=1) = \frac{qV}{W}$. This equation is a convenient form for numerical analysis with a boundary value solver. To put it into the form used in the Jaffé paper, we make the further substitution

$$h = 2\sqrt{K}g. \tag{2.5}$$

To compare with Jaffé's analysis, we denote his equation numbers with "(J-n)". In Equation (J-6), his "ξ" is our "h", and his "η" is our "$-f$". The reason for the sign change is that he "hard-wires" his analysis for $q = -e$. Doing a first integration of the resulting 2nd-order ODE, we get

$$\frac{df}{dh} = \pm[(1-f)^{1/2} + \alpha_1]^{1/2}, \tag{2.6}$$

where α_1 is an integration constant. This is Equation (J-7), except for the sign of f. Next, make the further substitution

$$u = (1-f)^{1/2}. \tag{2.7}$$

This transforms Equation (2.6) into

$$2u\frac{du}{dh} = \mp(u+\alpha_1)^{1/2}. \tag{2.8}$$

Finally, this can be integrated to give

$$F(u) = \tfrac{4}{3}(u-2\alpha_1)(u+\alpha_1)^{1/2} = \mp h + \alpha_2, \tag{2.9}$$

where α_2 is a second constant of integration. Except for the sign of h, this is Equation (J-9). Note that it is critically important that the plus sign in Equation (2.6) corresponds to the negative sign in Equations (2.8) and (2.9), and *vice versa*.

Equations (2.6), (2.8) and (2.9) are defined on the domain $0 \le h \le h_d$, where $h_d \equiv h(d) = 2\sqrt{K}$. Our variable h_d is Jaffé's ξ_0. The unknowns α_1 and α_2 are determined from the boundary conditions,

$$f(0) = 0, \text{ and } f(h_d) = f_d \equiv \frac{qV}{W}, \tag{2.10}$$

$$u(0) = 1, \text{ and } u(h_d) = u_d \equiv (1-f_d)^{1/2}. \tag{2.11}$$

Our u_d is Jaffé's u_0. We are interested in solutions for either an accelerating potential $f_d < 0$, or a grounded gap with $f_d = 0$. This leads to two possibilities for the profile $f(h)$, as shown qualitatively in Figure 2-1:

1. $f(h)$ mononotically decreases over the domain of h. This is a "Child-Langmuir-like" solution where $|qV| >> W$.
2. There is a local maximum in $f(h)$ at $h = \delta$. This is a "beam-like" solution when $|qV|$ is not as large compared to W.

Jaffé analyzes both of these cases, and also the decelerating potential case $f_d > 0$. In this report, we consider only Case 2, since this is the one with most relevance for photo-electrons injected into a cavity or a high velocity beam entering a drift section through a foil simulations. Here, $\frac{df}{dh} \ge 0$ and $\frac{du}{dh} \le 0$ for $0 \le h \le \delta$. Integrating Equation (2.8) between $0 \le h \le \delta$ using the minus sign, $F(u_\delta) - F(1) = -\delta$. But $F(u_\delta) = 0$ from Equation (2.8), so

$$\delta = \tfrac{4}{3}(1-2\alpha_1)(1+\alpha_1)^{1/2}. \tag{2.12}$$

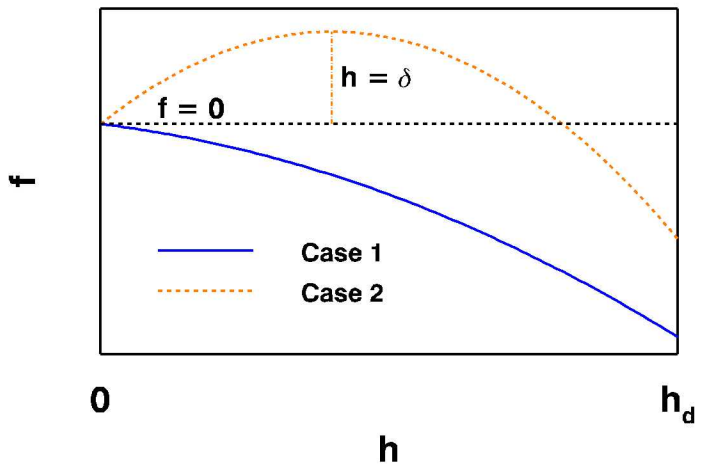

Figure 2-1. The two cases for $f(h)$ with $f_d \leq 0$.

Having obtained δ, it is immediately apparent that $\alpha_2 = \delta$, since $F(u_\delta) = 0$. We must choose the minus sign for h in the region $h \leq \delta$ and plus sign for $h > \delta$ to have the correct slopes. This gives

$$F(u) = \tfrac{4}{3}(u - 2\alpha_1)(u + \alpha_1)^{1/2} = \delta - h \ \ (h \leq \delta), \tag{2.13}$$

$$F(u) = \tfrac{4}{3}(u - 2\alpha_1)(u + \alpha_1)^{1/2} = h - \delta \ \ (h > \delta). \tag{2.14}$$

Finally, the boundary condition at $h = h_d$ determines the last unknown, α_1,

$$\tfrac{4}{3}(u_d - 2\alpha_1)(u_d + \alpha_1)^{1/2} + \tfrac{4}{3}(1 - 2\alpha_1)(1 + \alpha_1)^{1/2} = h_d. \tag{2.15}$$

Real solutions are only possible for $-1 \leq \alpha_1 \leq 0$. In the standard forward calculation to compute $\phi(x)$, we are given h_d and u_d. We first determine α_1 from Equation (2.15). Next, we compute δ from Equation (2.12), and then $u(h)$ from Equations (2.13) and (2.14). Finally, we back-substitute to obtain $f(g)$ and $\phi(x)$. This can only be done using a numerical root solver.

Jaffé demonstrates the existence of a maximum possible current in the following clever way. Instead of the forward calculation, assume that we are given u_d, and analyze the function $h_d(\alpha_1)$ in Equation (2.15). This function has a single maximum value in the allowed range $-1 \leq \alpha_1 \leq 0$ (see Jaffé's Figure 1). This maximum is located where $\frac{\partial h_d}{\partial \alpha_1} = 0$, which is at

$$\alpha_{1,max} = -\frac{u_d}{u_d + 1}. \tag{2.16}$$

The corresponding maximum value of h_d for a given u_d is thus

$$h_{d,max} = \tfrac{4}{3}(1+u_d)^{3/2}. \tag{2.17}$$

The resulting maximum current is

$$J_{max} = \frac{J_0}{4}\left[1+\left(1-\frac{qV}{W}\right)^{1/2}\right]^3. \tag{2.18}$$

It is remarkable that we have such a simple closed form for J_{max}, given how complicated the solution of the potential profile is. One other quantity of interest with a simple closed form is the maximum value of the potential. From Equation (2.6), Setting $\frac{df}{dh} = 0$ gives

$$f_{max} = 1-\alpha_1^2. \tag{2.19}$$

This is true for any α_1. Substituting Equation (2.16) into this, the greatest possible value of f_{max} is

$$f_{max}(J_{max}) = 1-\frac{u_d^2}{(1+u_d)^2} \tag{2.20}$$

In particular, for a grounded box, $u_d = 1$, and $f_{max}(J_{max}) = 0.75$. This shows that the particle velocity does **not** go to zero at $x = d/2$ at $J = J_{max}$.

As a basic test of theory, we consider the case of 10 keV electrons emitted across a 1 cm gap, with an applied potential of 5 keV. The emitted current is $J = 0.99999J_{max}$. This problem has also been analyzed with a numerical boundary value solver for Eq. (2.3) (originally developed for a related application). The good agreement between the potential profile from the two calculations is shown in Figure 2-2.

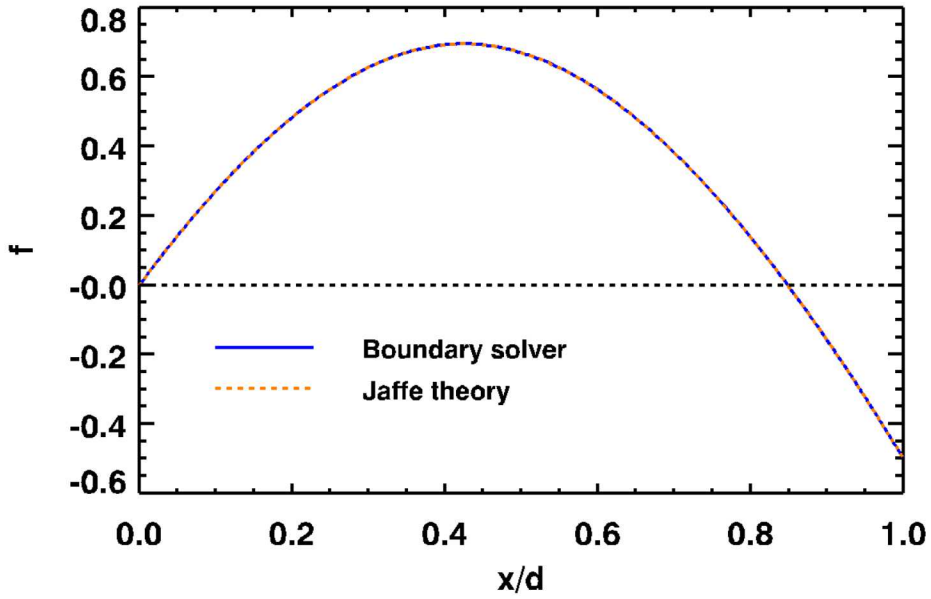

Figure 2-2. Comparison of the normalized potential profile $f(g)$.

3. VERIFICATION

In this section we will use the cold diode as a verification problem for the particle-in-cell code EMPIRE-PIC. Because there exists an analytic solution, outlined in the previous section, (Jaffé [1]), we can construct the "exact" solution for the electric potential (ϕ), electric field (E-field), electron velocity (v), and electron number density (n_e). The branch of the solution we will simulate holds the potential at the left side $V(0) = 0$ and at the right side $x = d$, at $V = 0$. The diode gap is $d = 0.01\ m$, the emitted particles all have the same energy $W = 10\ keV$ and the current density is $J = J_{max}/2 = 9.33582e4\ A/m^2$. For these conditions, we expect an equilibrium (steady-state) solution to exit. Starting at $time = 0$, particles are emitted from the left boundary with energy W. The particles cross the gap and are absorbed at the right boundary. The simulations continue until an equilibrium is reached.

EMPIRE-PIC uses a bi-linear or tri-linear Galerkin finite element method and an electrostatic assumption to solve Equation 1.3 for electric potential at nodes. The expected order of spatial convergence is therefore $p = 2$. The electric field is then reconstructed by projection of the gradient of the potential and also has an expected convergence $p = 2$. Particle positions and velocities are evolved in time using explicit time integration such as Leapfrog and Velocity-Verlet algorithms which are both order (Δt^2) algorithms. For very small temporal error, spatial accuracy is linked to the field accuracy and so it is expected to be $p = 2$ also.

In order to verify that EMPIRE-PIC is achieving the expected order of accuracy, we first define an error as the absolute difference between the analytic and computed solutions,

$$e_i = |U(x_i) - u(x_i)| \tag{3.1}$$

where U is the analytic value from the Jaffé solution and u is the computed value. The variable u may be electric potential, electric field, cell averaged velocity or particle velocity. The value $0 \leq x_i \leq d$ may be a mesh node, element center or particle location. Next, three discrete error norms are computed for each quantity of interest (QOI): L_1, L_2 and L_∞

$$\begin{aligned} L_1 &= \frac{1}{N}\sum_i e_i \\ L_2 &= \sqrt{\frac{1}{N}\sum_i (e_i)^2} \\ L_\infty &= \max_i (e_i) \end{aligned} \tag{3.2}$$

where N is either the number of cells in the x direction or the number of particles in a set of cells that span the distance from $x = 0$ to $x = d$.

Finally, the rate of convergence is defined as

$$p = \frac{log_e(u_c/u_f)}{log_e(h_c/h_f)} \tag{3.3}$$

where u_c, u_f are are error norms from a "coarse" and "fine" mesh respectively, and h_c, h_f are measures of the coarse and fine meshes respectively (typically, Δx). In all the computations presented here, u_c and u_f correspond to error norms from the simulations on four different meshes and $h_c/h_f = 2$.

EMPIRE-PIC solves the one-dimensional cold diode problem on two-dimensional meshes. Particles are emitted from a single location on a boundary cell face. Therefore, the electrons traversing the gap form a single beam. All of the verification tests use the solution at the last timestep. It was discovered that if the timestep is chosen arbitrarily, the convergence rate is degraded. The problem is that if the timestep is not an exact integer divisor of the transit time across the gap, the equilibrium PIC solution can never be symmetric about $x = d/2$. Furthermore, in the last $x-$cell, there will be a gap with no particles near $x = d$, further enhancing the asymmetry. Therefore, a transit time τ, has been defined, computed from the analytic solution

$$\tau = \int_{x=0}^{x=d} \frac{1}{v(x)} dx. \tag{3.4}$$

The simulation timestep is then chosen as an exact integer divisor of τ. While this may seem somewhat artificial, it is essential for convergence studies.

The verification tests are performed using two particle emission strategies. The first strategy is referred to as uniform particle emission and the second is random particle emission. For uniform emission, particles are emitted from the left boundary as a single beam at uniform sub-timestep-intervals. For random particle emission, particles are emitted as a single beam at random within uniform-timestep-intervals. The results are presented first for uniform particle emission followed by random particle emission.

3.1. UNIFORM PARTICLE EMISSION

The cold diode problem is solved by EMPIRE-PIC on two-dimentional meshes. The computational domain is a Cartesian rectangle, $x = [0, 0.01]\ m, y = [0, 0.0002]\ m$. All simulations in this section maintain the same y extent and use just two elements in the y-direction. Boundary conditions in the y-direction are periodic. Potential field boundary conditions are specified as Dirichelet with $V(0) = 0$, $V(x = d) = 0$. Particle boundary conditions are beam injection on the left, and absorbing on the right. Details of the simulations for uniform particle emission are shown on Table 3-1. The transit time

Table 3-1. Uniform particle emission simulation details.

$Mesh,\ N_x$	Δt	$N_p/\Delta t$	N_t	$\approx N_p$
800	$\Delta t/8$	32	64,000	192,000
400	$\Delta t/4$	16	32,000	48,000
200	$\Delta t/2$	8	16,000	12,000
100	Δt	4	8,000	3,000

computed from Equation 3.4, is $\tau = 1.8514280954e-10$ *sec* and the final time for all four simulations was $T_f = 1.97485663509e-09$ *sec*. The timestep (Δt) was chosen based on a Courant number constraint

$$CFL = \Delta t \frac{v}{\Delta x} \tag{3.5}$$

and since the timestep and cell size are reduced by one half with each mesh resolution level, the CFL remains roughly constant at $CFL \approx 0.13 - 0.15$ and the number of timesteps for the simulation N_t was doubled. The number of particles emitted per timestep $N_p/\Delta t$ was doubled for each mesh refinement level resulting in a factor of four increase in the total number of particles in the mesh N_p (for a single row of elements).

Convergence of the E-field at left and right boundaries serves as an indicator for equilibrium. An example is shown in Figure 3-1 for the coarse mesh $N_x = 100$.

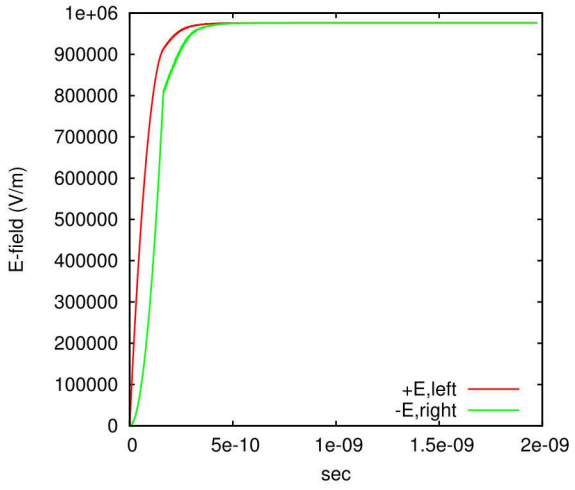

Figure 3-1. Time evolution of electric field at left and right boundaries for $N_x = 100$.

EMPIRE-PIC solutions for potential, E-field, electron number density, and velocity for four mesh resolution levels compared with the analytic solution are shown on Figure 3-2. Potential and E-field solutions are represented at mesh nodes, n_e and v are cell averages of

particles within each cell. Accept for n_e, which is rasterized due to the discrete number of particles, the profiles seem to indicate that mesh convergence has been achieved. An illustrative example of mesh convergence will is shown in Figure 3-3. In this case it is the potential at $x/d = 0.5$ where the potential reaches a minimum. With each level of refinement the computed solution approaches the analytic solution. Particle velocity profiles are much smoother than n_e due to the variation of v for each particle.

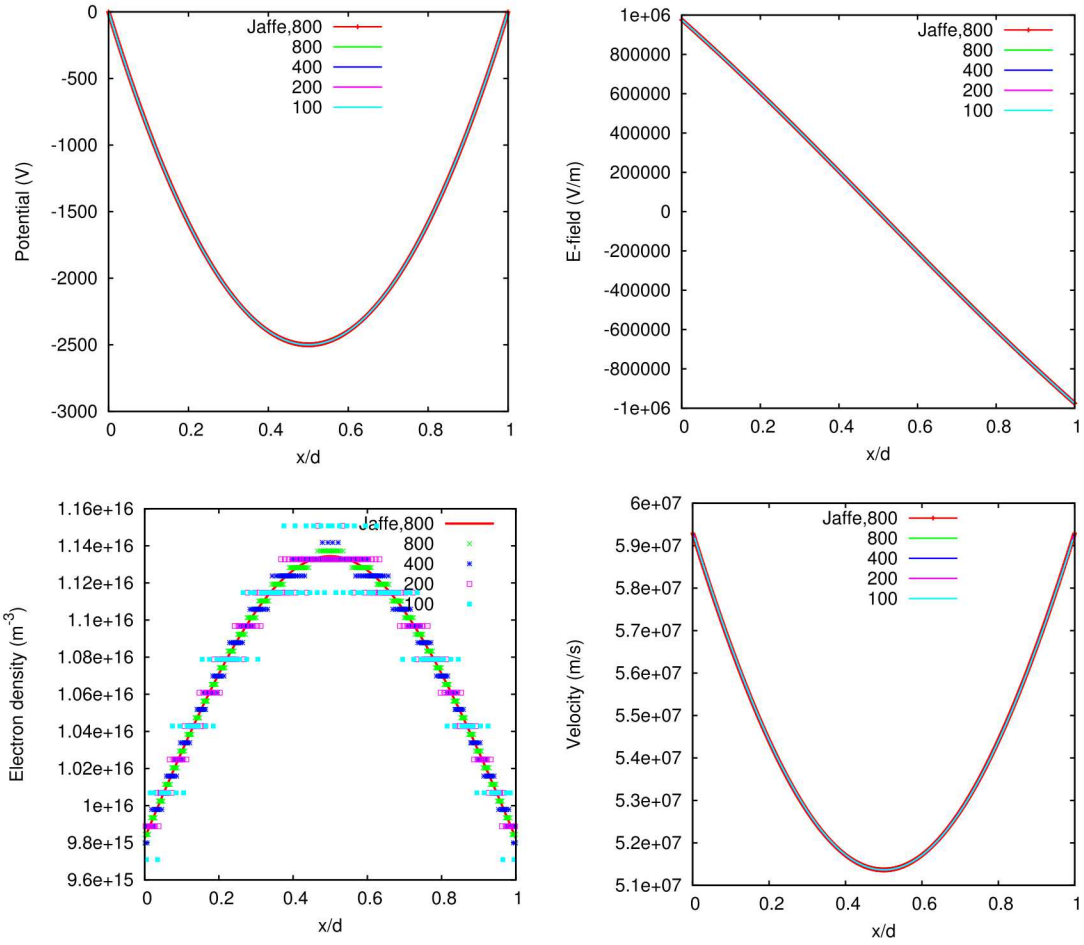

Figure 3-2. Comparison of computed solutions on four mesh levels with analytic solution (top left, potential; top right E-field; bottom left, electron number density; and bottom right, velocity).

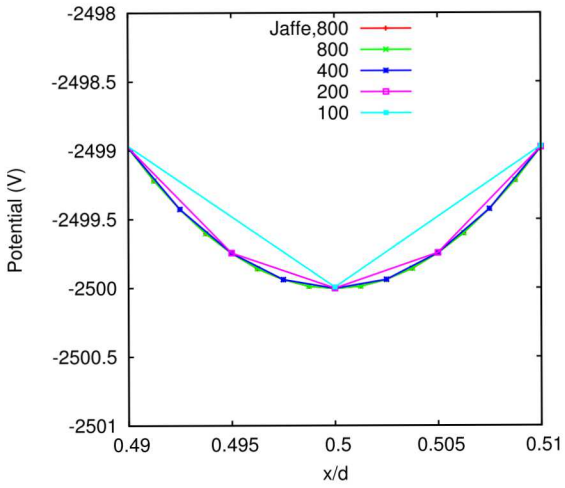

Figure 3-3. Expanded view of potential at $x/d = 0.5$ for four mesh levels.

Table 3-2. Potential convergence for uniform particle emission.

$Mesh$	L_1	L_2	L_∞
800	1.04371e-04	1.16270e-04	1.65664e-04
400	3.95097e-04	4.40798e-04	6.29765e-04
200	1.54530e-03	1.72740e-03	2.47874e-03
100	6.02472e-03	6.77347e-03	9.82517e-03

$Mesh\ pair$	L_1	L_2	L_∞
800-400	1.92048	1.92264	1.92656
400-200	1.96761	1.97041	1.97672
200-100	1.96301	1.97129	1.98688

3.1.1. Potential convergence

Electrical potential is a QOI that that has been verified. The potenial is the solution to the Poisson equation (Equation 1.3).

Table 3-2 presents the error norms (on the left) and convergence rates (on the right). The convergence rates are close to the expected order $p \approx 2$, however, there is a slight degradation in the rates as the mesh is refined. This behavior is unexpected and may be an indication of an as yet undetermined source of error. Figure 3-4 shows the potential error e_i (Equation 3.1) for the four mesh refinement levels (left) and the a plot of the error norms in log-log scale (right). Since Dirichlet boundary conditions for the potential are enforced, the error is zero on the boundaries.

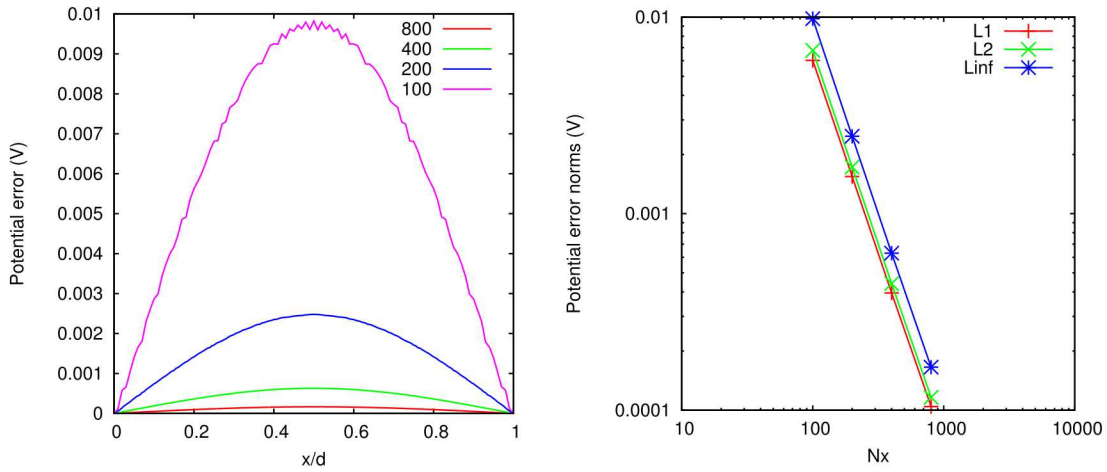

Figure 3-4. Potential errors and error norms four mesh levels.

3.1.2. E-field correction and convergence

For electrostatic simulations, the E-field is constructed from the potential solution

$$E = -\frac{d\phi}{dx}.$$

Table 3-3. E-field error norms and convergence slopes before boundary correction.

Mesh	L_1	L_2	L_∞
800	3.20527e+00	5.55599e+01	1.11185e+03
400	1.28024e+01	1.57158e+02	2.22517e+03
200	5.11027e+01	4.44575e+02	4.45619e+03
100	2.03628e+02	1.25781e+03	8.93590e+03

Mesh pair	L_1	L_2	L_∞
800-400	1.9979	1.5001	1.00095
400-200	1.99698	1.50021	1.0019
200-100	1.99446	1.50041	1.0038

Early investigations produced convergence rates that were lower than expected (shown in Table 3-3). The problem was traced to the boundary values as can be seen in Figure 3-5 (left). This large error, confined to the boundary nodes, affects the error norms differently (see Figure 3-5, right), resulting in $p \approx 1$ convergence of L_∞, $p \approx 1.5$ for L_1 and $p \approx 2$ for the L_2. Since the L_2 norm represents an average over the entire domain (see Equation 3.2), two isolated large errors is not enough to significantly degrade convergence.

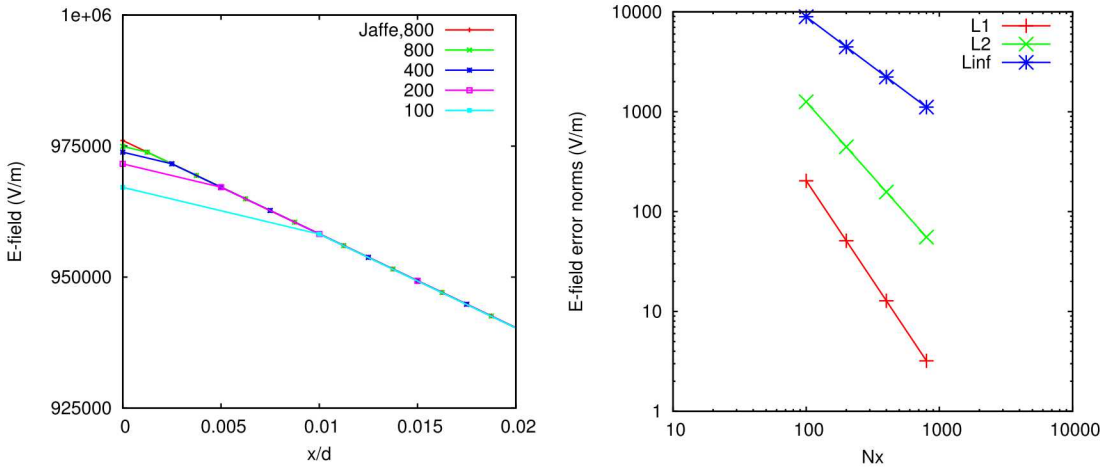

Figure 3-5. E-field at left boundary showing error and error norms for four mesh levels before boundary correction.

The problem at the boundary is that the value E_0 was simply being set with $E_{1/2}$. In fact, careful examination of Figure 3-5 shows that if the point at $x = 0$ were moved to $x = \Delta x/2$, the slope would be relatively smooth. A much better way to extrapolate $E_{1/2}$ down to $x = 0$ is to use Gauss' Law, including the charge density at $x = 0$,

$$E_0 = E_{1/2} - \frac{\Delta x}{2}\frac{\rho_0}{\epsilon_0} = E_{1/2} + \frac{q_e n_0 \Delta x}{2\epsilon_0}. \tag{3.6}$$

This correction had been on the EMPIRE "wish list" for some time, since it is fairly complicated. The convergence study here first highlighted how important it can be. The verification test was re-run with this correction which resulted in much improved E-field

predictions. An expanded view of corrected E-field profiles at both left and right boundaries are shown in Figure 3-6 now showing good agreement with the analytic solution. Error norms and convergence rates are presented in Table 3-4 now showing the expected order of convergence in all three norms. Error profiles and error norms are shown in Figure 3-7. Notice that the boundary errors are greatly reduced compared even to interior values.

Table 3-4. E-field error norms and convergence slopes with boundary correction.

Mesh	L_1	L_2	L_∞
800	1.75919e-01	1.94761e-01	2.78353e-01
400	6.95440e-01	7.70235e-01	1.10889e+00
200	2.76023e+00	3.06044e+00	4.48785e+00
100	1.09072e+01	1.21456e+01	1.78924e+01

Mesh pair	L_1	L_2	L_∞
800-400	1.98302	1.98359	1.99414
400-200	1.98879	1.99037	2.0169
200-100	1.98242	1.98863	1.99525

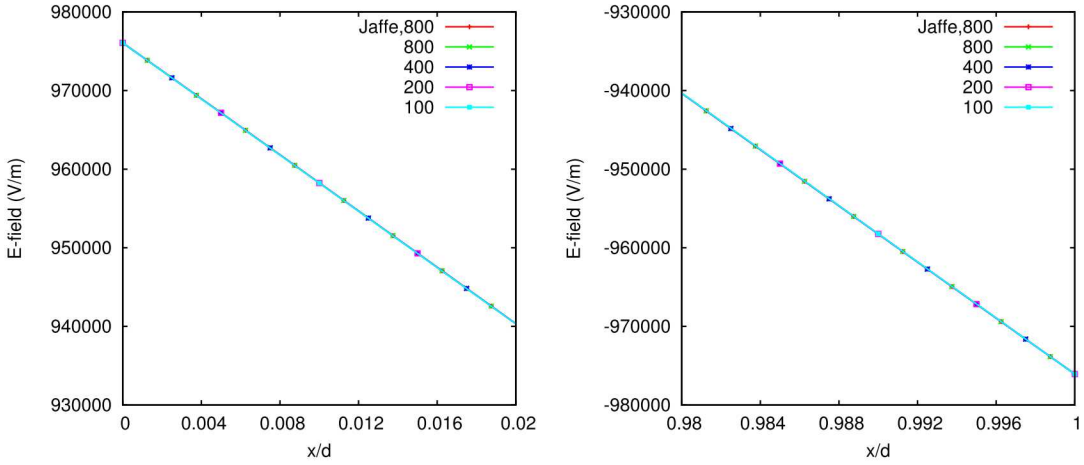

Figure 3-6. E-field at left and right boundaries for four mesh levels after boundary correction.

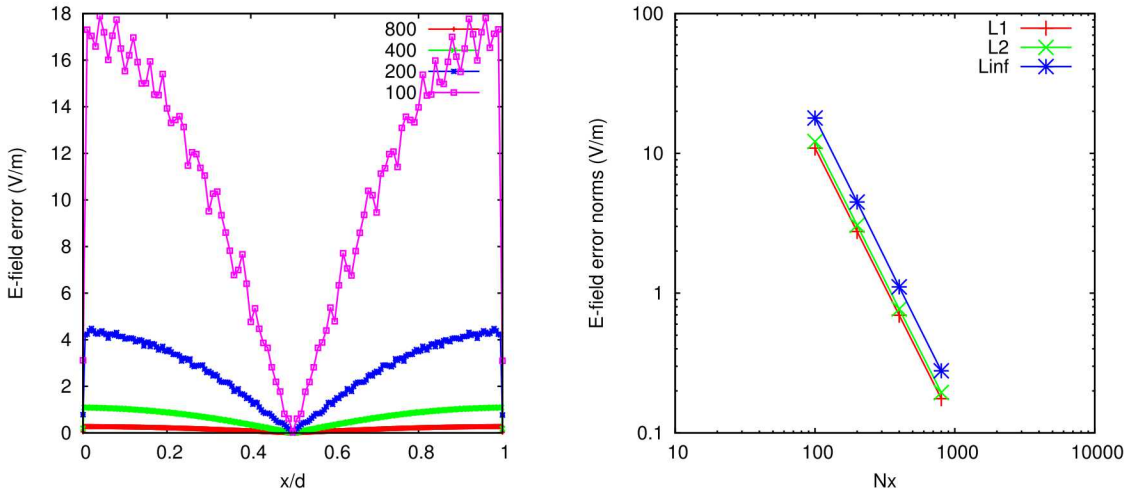

Figure 3-7. E-field error profiles and error norms after boundary correction.

3.1.3. Velocity correction and convergence

Evolution of individual particle positions and velocity are governed by the equation of motion

$$m_e \frac{\partial v(x)}{\partial t} = -q_e E(x) \tag{3.7}$$

where m_e is the electron mass, $-q_e$ is the electron charge and $E(x)$ is the electric field obtained from the solution to Poisson's equation. Particle acceleration is defined as

$$a(x) = -q_e E(x)/m_e. \tag{3.8}$$

Explicit time integration in EMPIRE-PIC utilized the second-order accurate Leapfrog algorithm

$$\begin{aligned} v_{n+1/2} &= v_{n-1/2} + \Delta t a(x_n) \\ x_{n+1} &= x_n + \Delta t v_{n+1/2} \end{aligned} \tag{3.9}$$

where $n-1/2$, n, $n+1/2$, and $n+1$ are timestep indices. Notice that position and velocity are staggered in time. While it has been assumed that PIC solutions are steady, it is important to realize that accuracy in potential and E-field depend on particles being at right location and accuracy in the velocity requires that the particles be at the right location with the right velocity at the right time. Particle location and velocity written to output data files were out of sync by a half timestep. This resulted in large error norms and sub-optimal ($p \approx 1$) convergence slopes. Error norms and convergence slopes are presented for the cell averaged velocity in Table 3-5 and individual particles in Table 3-6 respectively. Notice also that the error norms for individual particles are smaller than error norms for cell averaged velocities. Because of this, the individual particle velocity only will be reported in the rest of the report.

Table 3-5. Cell velocity error norms and convergence slopes.

Mesh	L_1	L_2	L_∞
800	1.35678e+03	1.55909e+03	2.69123e+03
400	2.71490e+03	3.12009e+03	5.42524e+03
200	5.42865e+03	6.24420e+03	1.15129e+04
100	1.08368e+04	1.25257e+04	2.30822e+04

Mesh pair	L_1	L_2	L_∞
800-400	1.00071	1.00089	1.01142
400-200	0.999696	1.00093	1.0855
200-100	0.997273	1.0043	1.00352

A correction of the form

$$\delta V(x_i) = \frac{q_e \Delta t}{2 m_e} E(x_i) \tag{3.10}$$

Table 3-6. Particle velocity error norms and convergence slopes.

$Mesh$	L_1	L_2	L_∞
800	1.32434e+03	1.52921e+03	2.64894e+03
400	2.64869e+03	3.05844e+03	5.29764e+03
200	5.29753e+03	6.11700e+03	1.05951e+04
100	1.05962e+04	1.22349e+04	2.11903e+04

$Mesh\ pair$	L_1	L_2	L_∞
800-400	1.00001	1.00001	0.999936
400-200	1.00004	1.00003	0.999973
200-100	1.00016	1.00011	1.00001

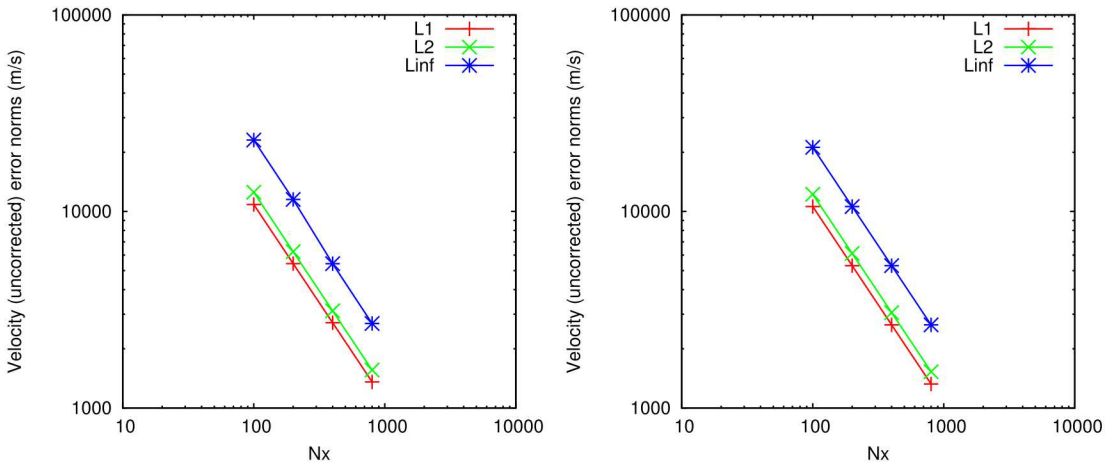

Figure 3-8. Cell averaged and particle velocity error norms four mesh levels.

Table 3-7. Corrected particle velocity error norms and convergence slopes.

Mesh	L_1	L_2	L_∞
800	3.07685e+00	3.34104e+00	4.74233e+00
400	1.15088e+01	1.26309e+01	1.81626e+01
200	4.51018e+01	4.96648e+01	7.16458e+01
100	1.78667e+02	1.97023e+02	2.83348e+02

Mesh pair	L_1	L_2	L_∞
800-400	1.90322	1.91859	1.9373
400-200	1.97044	1.97527	1.97991
200-100	1.98602	1.98807	1.98362

where V_i and $E(x_i)$ are the analytic values of the velocity and E-field respectively, can be applied to the analytic solution. Using a slightly different definition of the error,

$$e_i = |(V(x_i) + \delta V(x_i)) - v(x_i)| \tag{3.11}$$

the expected order of convergence is achieved as shown in Table 3-7 and Figure 3-9.

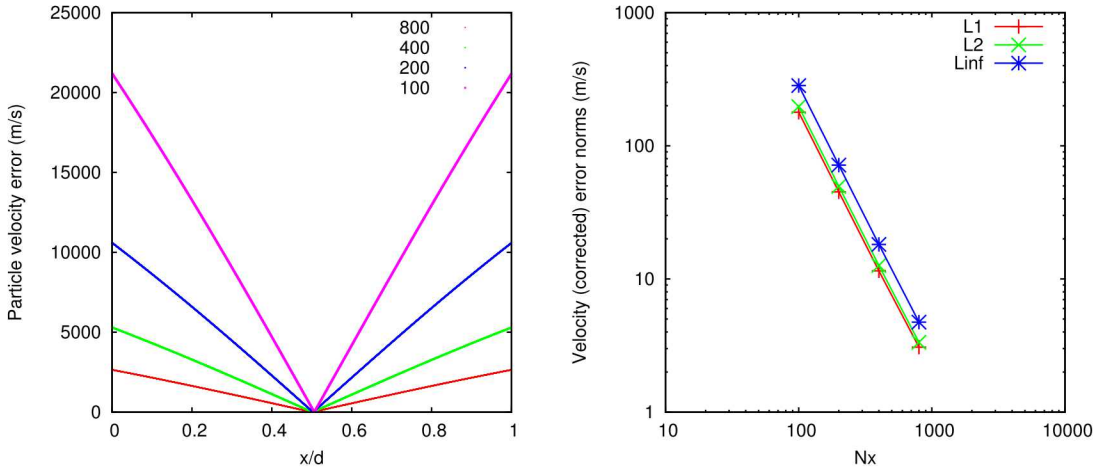

Figure 3-9. Corrected particle velocity error profiles and norms for four mesh levels.

3.1.4. Velocity-Verlet time integration

The requirement to "correct" for the out-of-sync position with velocity, can be alleviated by adopting a different time integration algorithm. Velocity-Verlet is an explicit second-oder accurate time integration scheme that does not require a correction - particle position and velocity are in sync and can be written to output data files as such. The algorithm for the one-dimensional diode problem is

Table 3-8. Particle velocity error norms and convergence slopes for Velocity-Verlet time integration.

$Mesh$	L_1	L_2	L_∞
800	3.07685e+00	3.34104e+00	4.74233e+00
400	1.15088e+01	1.26309e+01	1.81626e+01
200	4.51018e+01	4.96647e+01	7.16457e+01
100	1.78668e+02	1.97023e+02	2.83347e+02

$Mesh\ pair$	L_1	L_2	L_∞
800-400	1.90322	1.91859	1.9373
400-200	1.97044	1.97527	1.97991
200-100	1.98602	1.98807	1.98362

$$
\begin{aligned}
v_{n+1/2} &= v_n + \frac{\Delta t}{2} a(x_n) \\
x_{n+1} &= x_n + \Delta t v_{n+1/2} \\
v_{n+1} &= v_{n+1/2} + \frac{\Delta t}{2} a(x_{n+1}).
\end{aligned}
\tag{3.12}
$$

The verification test was run with Velocity-Verlet time integration. All parameters were kept the same as for Leapfrog integration. Error norms and convergence slopes for solutions using Velocity-Verlet are shown in Table 3-8 and plots of error profiles and error norms are presented in Figure 3-10. Notice the close agreement between Leapfrog and Velocity-Verlet by comparing Tables 3-7 and 3-8.

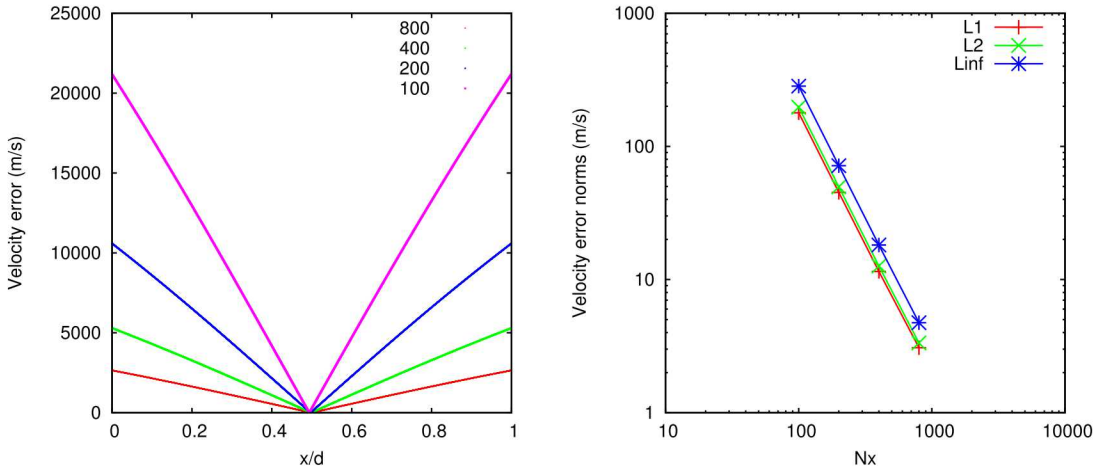

Figure 3-10. Particle velocity error profiles and norms for four mesh levels using Velocity-Verlet time integration.

3.2. RANDOM PARTICLE EMISSION

Details of the simulations for random particle emission are shown on Table 3-9. For random particle emission, the simulation details are very similar to the uniform simulations with the exception of the number of particles emitted per timestep $N_p/\Delta t$. In the random emission simulations: T_f, τ, Δt and N_t were the same as in the uniform emission simulations. All boundary conditions were kept the same as in uniform emission simulations. In the random cases, the number of emitted particles was required to be much greater in order to establish convergence which lead to a much greater total number of particles N_p.

Table 3-9. Random particle emission simulation details.

$Mesh,\ N_x$	Δt	$N_p/\Delta t$	N_t	$\approx N_p$
800	$\Delta t/8$	256	64,000	1,536,000
400	$\Delta t/4$	256	32,000	768,000
200	$\Delta t/2$	256	16,000	384,000
100	Δt	256	8,000	192,000

3.2.1. Convergence with varying number of emitted particles

Convergence rates for random emission are expected to be a bit "noisier" than for the uniform emission simulations. In order to give some idea of how the convergence rates for the three QOI: potential, E-field and particle velocity, are affected by the number of particles emitted, Tables 3-10, 3-11 and 3-12 present the convergence rates for varying number of emitted particles per timestep. While rates do not improve monotonically with N_p, the general trend for all QOI is that the rates increase with N_p.

Table 3-10. Potential convergence slopes of the 800-400 mesh pair for varying number of emitted particles.

$N_p/\Delta t$	L_1	L_2	L_∞
256	1.92513	1.92599	1.92297
128	1.9217	1.9246	1.93053
64	2.00036	1.99775	1.99503
32	1.77714	1.74558	1.6219
16	1.33498	1.3778	1.52273
8	2.22636	2.09628	1.85115
4	3.36529	3.20131	2.43048

Table 3-11. E-field convergence slopes of the 800-400 mesh pair for varying number of emitted particles.

$N_p/\Delta t$	L_1	L_2	L_∞
256	1.98215	1.98379	1.96714
128	1.98338	1.98223	1.92875
64	1.99385	1.98479	1.71293
32	1.87454	1.8604	1.71281
16	1.59524	1.51827	1.43271
8	1.19685	1.17436	1.05366
4	1.02005	1.01082	1.0855

Table 3-12. Velocity convergence slopes of the 800-400 mesh pair for varying number of emitted particles.

$N_p/\Delta t$	L_1	L_2	L_∞
256	1.90333	1.91778	1.90505
128	1.90301	1.91787	1.91545
64	1.90301	1.91787	1.91545
32	1.90195	1.86827	1.49328
16	1.56451	1.47682	1.46173
8	1.29817	1.2181	0.802471
4	0.869544	0.801669	0.364038

3.2.2. Convergence of QOIs

Using $N_p/\Delta t = 256$ for all mesh refinement levels, error norms and convergence slopes for potential, E-field and particle velocity were computed and are shown in Tables 3-13, 3-14 and 3-15 respectively. In all three QOI, the three norms are converging at ($p \approx 2$), the expected order of convergence. Error norms are plotted for the three QOI in Figure 3-11.

Table 3-13. Potential error norms and convergence slopes for random particle emission.

Mesh	L_1	L_2	L_∞
800	1.03966e-04	1.15813e-04	1.65368e-04
400	3.94834e-04	4.40086e-04	6.27082e-04
200	1.54977e-03	1.73186e-03	2.48001e-03
100	6.11689e-03	6.84980e-03	9.81825e-03

Mesh pair	L_1	L_2	L_∞
800-400	1.92513	1.92599	1.92297
400-200	1.97273	1.97646	1.98362
200-100	1.98075	1.98374	1.98512

Table 3-14. E-field error norms and convergence slopes for random particle emission.

Mesh	L_1	L_2	L_∞
800	1.75860e-01	1.94650e-01	2.80949e-01
400	6.94793e-01	7.69902e-01	1.09848e+00
200	2.76477e+00	3.06218e+00	4.38988e+00
100	1.09480e+01	1.21497e+01	1.74094e+01

Mesh pair	L_1	L_2	L_∞
800-400	1.98215	1.98379	1.96714
400-200	1.99251	1.99181	1.99867
200-100	1.98543	1.98829	1.98761

Table 3-15. Velocity error norms and convergence slopes for random particle emission.

Mesh	L_1	L_2	L_∞
800	3.07585e+00	3.34173e+00	4.89064e+00
400	1.15060e+01	1.26264e+01	1.83165e+01
200	4.50952e+01	4.96415e+01	7.16766e+01
100	1.78241e+02	1.96669e+02	2.84867e+02

Mesh pair	L_1	L_2	L_∞
800-400	1.90333	1.91778	1.90505
400-200	1.97059	1.9751	1.96836
200-100	1.98279	1.98615	1.99071

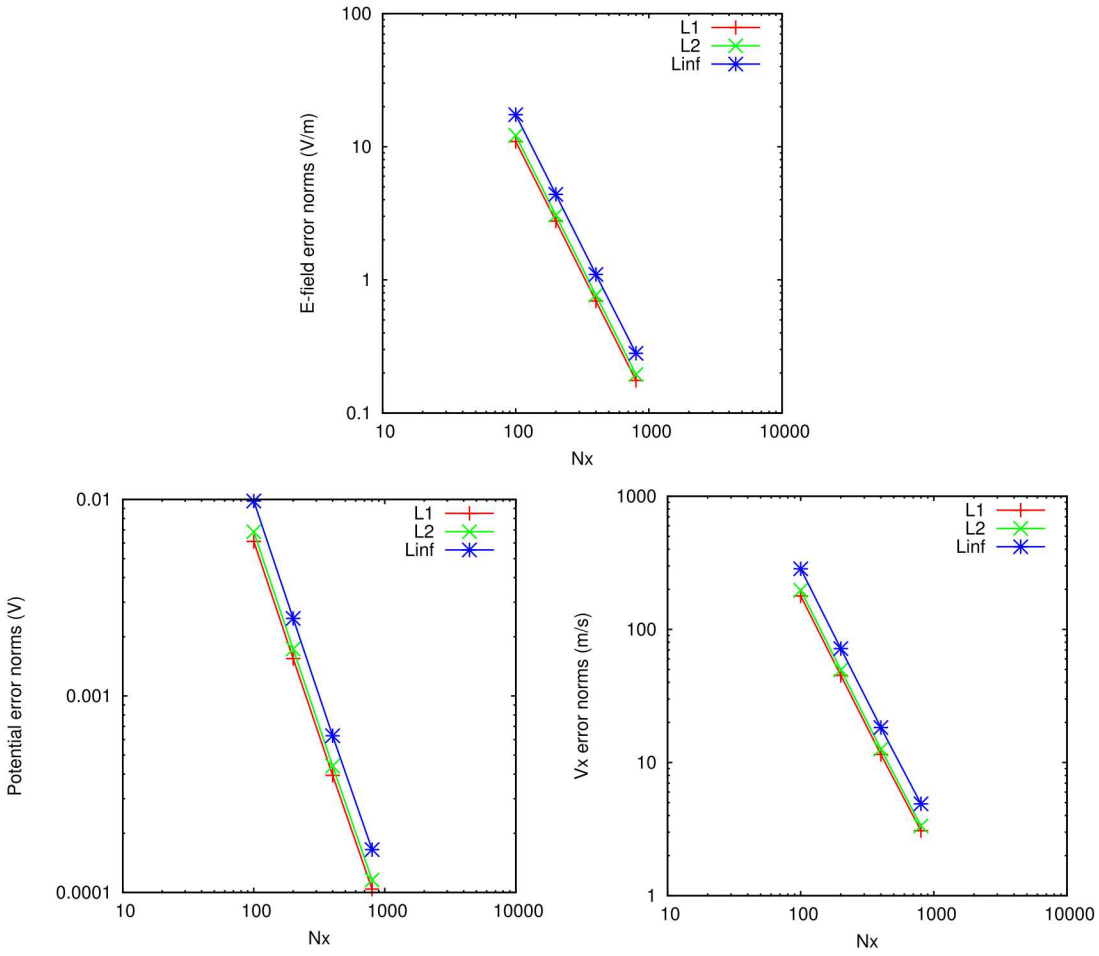

Figure 3-11. Error norms for random particle emission for four mesh levels. Top, E-field; bottom left, potential; bottom right, particle velocity.

4. DISCUSSION

The cold diode differs from the "warm" diode in one important aspect. That is the thermal velocity usually associated with electron emission from a surface. Thermal velocities are three-dimensional, random, and usually conform to a Maxwellian distribution. This randomness (as we saw in the Section 3.2 on random particle emission can make verification more difficult due to the inherent non-smoothness introduced by the random behavior. Nevertheless, the cold diode simulation is an attractive verification problem because the randomness can be eliminated or at least greatly removed from the simulation. The electron beam is in a sense mimicing or approaching a continuous (one-dimentional) field, as the number of emitted particles is increased, allowing for the use of mesh convergence techniques to verify a PIC code, typically used to verify fluid codes. Random particle emission may require more particles be emitted per timestep to reduce the non-smoothness of the beam compared with uniform particle emission.

Specifying that the timestep be an integral divisor of the transit time contributes to the continuum approximation and reduces the required number of emitted particles. Expected order accuracy, in the case of uniform particle emission, using this transit time based timestep was achieved with very few particles emitted per timestep compared to the number required by random particle emission.

A different approach to verifying a PIC code could involve ensemble averaging over multiple steady solutions. In this way the randomness would be smoothed by the averaging process. While that may be an acceptable strategy for steady problems like the cold diode, many problems of interest are inherently transient so in these cases, it is very important to establish code accuracy that corresponds to problems of interest. The code diode problem is good example of this type of test problem.

5. CONCLUSIONS

The cold diode is an excellent problem for formal verification of PIC codes because: there exists a relatively simple analytic solution so code errors can be accuately assessed, noise associated with random particle motion can be greatly reduced therefore reducing computational cost, and by emitting particles as a beam, smooth "fluid like" solutions are obtained allowing well established continuum code verification techniques to be used. Using the cold diode problem the electric potential, E-field and particle velocity solutions were verified to converge at the expected spatial order of accuracy. This implies that (at least for this problem) the electrostatic field solver, boundary conditions and time integrators are correctly implemented.

An error in the projected E-field at boundaries was identified and once corrected allowed the expected order of accuracy for all three norms to be achieved. It was necessary to apply a correction to the error for Leapfrog time integration in order to achieve expected order of accuracy. The Velocity-Verlet time integration algorithm was also verified using this problem. Finally, random particle emission was also verified and expected orders of convergence of solutions were achieved albeit with far greater numbers of emitted particles.

BIBLIOGRAPHY

[1] George Jaffé. On the currents carried by electrons of uniform initial velocity. *Physical Review*, 65(3):91–98, 1944.

[2] Loup Verlet. Computer "experiments" on classical fluids. i. thermodynamical propertie s of Lennard-Jones molecules. *Phys. Rev.*, 159:98–103, July 1967.

[3] C.D. Child. Discharge from hot CaO. *Physical Review (Series I)*, 32:492, May 1911.

[4] I. Langmuir. The effect of space charge and residual gases on thermionic currents in high vacuum. *Physical Review*, 2:450, December 1913.

DISTRIBUTION

Hardcopy—External

Number of Copies	Name(s)	Company Name and Company Mailing Address

Email—Internal [redacted]

Name	Org.	Sandia Email Address
Technical Library	01177	libref@sandia.gov

Sandia National Laboratories is a multimission laboratory managed and operated by National Technology & Engineering Solutions of Sandia LLC, a wholly owned subsidiary of Honeywell International Inc., for the U.S. Department of Energy's National Nuclear Security Administration under contract DE-NA0003525.